



TECHNICAL ARTICLE

Hydrogen Embrittlement Behavior and Mechanism of Low Carbon Medium Manganese Steel Gas Metal Arc Welding Joints

Y. DU ^{1,2,4} X.H. GAO,^{2,5} X.N. WANG,^{1,6} Y. DONG,² B. ZHANG,²
H.Y. WU,² C. SUN,³ and L.X. DU²

1.—School of Iron and Steel, Soochow University, Suzhou 215021, Jiangsu, China. 2.—State Key Laboratory of Rolling and Automation, Northeastern University, Shenyang 110819, Liaoning, China. 3.—Nanjing Iron & Steel Co., Ltd., Nanjing 210035, Jiangsu, China. 4.—e-mail: duyu2022@suda.edu.cn. 5.—e-mail: gaoxh@ral.neu.edu.cn. 6.—e-mail: wxn@suda.edu.cn

The hydrogen embrittlement behavior of two low-carbon medium manganese steel welding joints was elucidated using a slow strain rate tensile experiment, hydrogen permeation experiment, and hydrogen concentration test. The fracture starting position becomes heat-affected zone (HAZ) after hydrogen charging. The hydrogen concentration of HAZ is higher than weld material (WM) for two welding joints after hydrogen charging for both 1 h and 2 h. The hydrogen embrittlement susceptibility of the welding joint with high hydrogen concentration, which contains about 0.03 Ti in both WM and HAZ, is larger than the welding joint that does not contain Ti. When the hydrogen charging time of the Ti-contained welding joints increases from 1 h to 2 h, the fractography of WM changes from small shallow dimples (hydrogen enhanced localized plasticity) to quasi-cleavage and cleavage (hydrogen enhanced decohesion), and the fractography of HAZ changes from quasi-cleavage (hydrogen enhanced decohesion) to intergranular (hydrogen enhanced decohesion).

INTRODUCTION

Hydrogen embrittlement (HE) is considered a severe issue of high-strength steel, essentially for welding joints of high-strength steel, because of its inhomogeneous microstructures and high internal stress.^{1,2} Many researchers found that the main influences of HE susceptibility are chemical composition, strength, residual stress value, and hydrogen concentration.^{3,4} Until now, two types of HE mechanisms have been established and widely accepted; one type is based on the viewpoint of “brittle,” including internal pressure theory and hydrogen enhanced decohesion (HEDE) theory, and the other type is based on the viewpoint of “ductile,” including hydrogen enhanced localized plasticity (HELP)

theory and adsorption induced dislocation emission (AIDE) theory.^{5–10} Essentially, these mechanisms involve the interaction between microstructures and hydrogen in steels.^{11–14}

Recently, low-carbon medium manganese steels have attracted significant attention due to their good tradeoff between mechanical properties and material cost.^{15–19} The toughness improvement was obtained via introducing metastable austenite by inter-critical annealing, which can stabilize at room temperature via enrichment of C and Mn.^{20–23} Martensite is generally recognized as one of the most sensitive phases to HE because of its high brittleness and hardness. However, retained austenite (RA) introduced by inter-critical annealing treatment is considered the most insensitive phase to HE.^{24–28} Until now, we have studied the HE of medium manganese steels and found that HE susceptibility is related to the dislocation density of martensite matrix and the stability of RA. However,

the microstructures of welding joints are very different from BM.^{29–31} Due to their chemical composition characteristics, medium manganese steels are difficult to weld. Therefore, the microstructures and mechanical properties of medium manganese steel welding joints are very important for applying medium manganese steel. Yoo has investigated the correlation between microstructure and mechanical properties of the heat-affected zone (HAZ) in Fe8Mn0.06C steel welding joints and found that the presence of RA contributed to an increase in toughness and a decrease in ductile-brittle transition temperature.³²

In addition, HE susceptibility is significant for the welded joints serviced in the marine environment. In particular, microstructures and hardness of HAZ have significant influences on HE.^{33–37} Zhang found the change in HE susceptibility from high to low was coarse-grained HAZ (CGHAZ), fine-grained HAZ (FGHAZ), inter-critical HAZ (ICHAZ), and base metal (BM) because lower hydrogen diffusivity can impede the embrittlement behavior.³³ In addition, several studies have described that hydrogen permeation behavior is essential to evaluate the HE of welding joints.^{34,35} Lan studied two welding joints with and without post-weld heat treatments and found that the tempered membranes have a lower effective diffusion coefficient and higher density of hydrogen traps due to newly formed carbides acting as hydrogen trapping sites.³⁶ Furthermore, medium manganese steels are often used to construct offshore platforms.^{37–40} Therefore, studying the hydrogen diffusion and HE behaviors of medium manganese steel welding joints is very significant. However, the hydrogen diffusion and HE behavior of medium manganese steel welding joints have rarely been studied.

In the present study, two high-strength medium manganese steel plates were welded using gas metal arc welding. The hydrogen permeation experiments were employed to study the relationship between hydrogen diffusion behavior and microstructures of welding joints. Slow strain rate tensile experiments of welding joints after different hydrogen charging times were employed to study the HE of welding joints. The concentrations after hydrogen charging for different weld metal (WM) and HAZ times were measured using the melt extraction method. The hardness of different welding joints was tested using a Vickers hardness tester to study the relationship between hardness and HE.

EXPERIMENTAL METHODS

Gas Metal Arc Welding Experiments

Two 30-mm-thick low carbon medium manganese steel plates (BM A and BM B) with different chemical compositions were studied using the gas metal arc welding method, where the welding wires corresponding to BM A and BM B are welded materials A

and B (WM A and WM B), respectively. The chemical compositions of the two BMs and WMs are shown in Table I; 0.031% and 0.036% Ti were added to BM A and WM A but not added to BM B and WM B. Another noticeable difference is that the Ni content of WM A is 3.39%, which is higher than that of WM B (2.21%). Hot-rolled plates of 30 mm thickness were heated to 820°C for half an hour, then water-quenched to room temperature, and the quenched steels were annealed at 630°C for half an hour to gain some RA. The microstructures of the two BMs are tempered martensite with about 25% RA, and the tensile properties of the two BMs are listed in supplementary Table SI (refer to online supplementary material).^{29,30} After pre-heating at 200°C, five passes of welding were performed on double bevel butts using the parameters: current 300 A, voltage 33 V, and welding speed 30 cm min⁻¹; shield gas was composed of 80% Ar and 20% CO₂, and the corresponding heat input was about 20 kJ cm⁻¹. Then, post-weld bake treatment was carried out for 120 min at 200°C and air cooled. The specimens of electrochemical hydrogen permeation experiments and slow strain rate tensile experiments were sampled from the welding plates after welding, as shown in supplementary Fig. S1.

Electrochemical Hydrogen Permeation Experiment

The hydrogen permeation experiment was carried out using a Fe-HP-12 hydrogen permeation tester based on the principle of the Devanathan-Stachurski double electrolysis cell, and the Fe-HP-12 hydrogen permeation tester met the standard ISO 17081-2014.⁴¹ Steel specimens are extracted from the surface of the welding joint and parallel to the rolling plane with the dimension of 50 × 80 × 1 mm³, as shown in supplementary Fig. S1, and the hydrogen charging area is circular, about 7.07 cm². The oxidation side of the membranes was electrochemically deposited with a nickel coating in an aqueous solution of 125 g L⁻¹ NiSO₄·7H₂O, 22.5 g L⁻¹ NiCl₂·6H₂O, and 20 g L⁻¹ H₃BO₃ at a current density of 10 mA cm⁻² for 1 min prior to mounting. Then, a constant potential of 250 mV (versus saturated calomel electrode) was applied on the oxidation side in a 0.1 M NaOH aqueous solution. Until the residual current density decreased to 2 μA cm⁻², the charging side was filled with 0.1 M NaOH + 1 M Na₂S aqueous solution,

Table I. Chemical compositions of two BMs and WMs (wt.%)

	C	Si	Mn	Mo	Ni	Ti
BM A	0.069	0.18	4.38	0.21	0.26	0.031
WM A	0.111	0.54	1.63	0.49	3.39	0.036
BM B	0.065	0.20	5.45	0.16	0.31	/
WM B	0.088	0.51	1.75	0.51	2.21	/

and a constant current density of 5 mA cm^{-2} was applied. Each welding joint can be regarded as a whole to analyze the effect of microstructures on hydrogen diffusion. This situation is closer to the actual engineering application environment of welding joints because almost all the welding joint should be covered in the exposed region (see supplementary Fig. S2). As this figure show, the width of WM is about 21 mm, and the exposed area mainly contains about 80% WM and 20% HAZ.

The permeation current (I), steady-state hydrogen permeation flux (J_{ss}), and time reaching a value of $J(t)/J_{ss} = 0.63$ (t_{lag}) were directly obtained from the hydrogen permeation oxidation current curves. Effective hydrogen diffusion coefficient (D_{eff}), hydrogen permeation flux (J), and the summation of the sub-surface concentration of hydrogen in interstitial lattice sites and reversible trap sites (C_{OR}) were calculated based on Eqs. 1, 2, and 3.⁴¹

$$D_{eff} = \frac{L^2}{6t_{lag}} \quad (1)$$

$$J(t) = \frac{I(t)/S}{F} \quad (2)$$

$$C_{OR} = \frac{J_{ss}L}{D_{eff}} \quad (3)$$

Here, S is the exposed area in the oxidation cell, F is the Faraday constant ($96,485 \text{ C mol}^{-1}$), and L is the thickness of specimens. Additionally, when the effect of hydrogen traps on hydrogen diffusion is dominant, the effective diffusion coefficient can be roughly expressed by the following equation.⁴²

$$D_{eff} = D_L \left(1 + \frac{3N_T}{N_A \cdot C_{OR}} \right)^{-1} \quad (4)$$

where N_T is the number of hydrogen trapping sites, N_A is Avogadro's constant, and D_L is the lattice diffusion coefficient reported as $9.5 \times 10^{-9} \text{ m}^2 \text{ s}^{-1}$ in pure iron.⁴³

Hydrogen Charging and Melt Extraction Experiments

To determine the hydrogen concentration in WM and HAZ of welding joints after different hydrogen charging, the melt extraction experiments were carried out using the LECO TCH-600 hydrogen analyzer. The specimens were taken in the same region as the reduced parallel section of tensile specimens. The specimens are cylinders with 6-mm diameter, which are the same size as the reduced parallel section. Hydrogen was electrochemically charged into the entire specimens in an aqueous solution of 5 vol.% H_2SO_4 containing 0.3 g L^{-1} NH_4SCN at 1 mA cm^{-2} for 1 h and 2 h at room temperature. After hydrogen charging, WM and HAZ were sampled for hydrogen concentration tests, respectively, and the time between hydrogen charging and melt extraction experiments was < 2

min. Meanwhile, to distinguish the concentration of diffusible hydrogen and trapped hydrogen, hydrogen concentration tests were also conducted after being exposed to air for 60 h.

Hydrogen Charging and Slow Strain Rate Tensile Experiment

Tensile specimens with 30-mm gage length and 6-mm diameter were prepared perpendicular to WM, and hydrogen charging conditions were the same as in the melt extraction experiment. The time between after hydrogen charging and slow strain rate tensile experiment was also within 2 min. Slow strain rate tensile tests were conducted on these specimens using the AG-XPLUS100KN universal testing machine at a constant strain rate of $6.7 \times 10^{-5} \text{ s}^{-1}$ at 298 K. The stress-strain curve is recorded, and the total elongation and reduction in the area after fracture are measured. Fractography observation was undertaken using a scanning electron microscope (SEM, FEI QUANTA 600) operated at 20 kV. Two embrittlement indexes were defined to evaluate HE susceptibility quantitatively:

$$EL_{loss} = \frac{EL_{uncharged} - EL_{charged}}{EL_{uncharged}} \times 100\% \quad (5)$$

$$RIA_{loss} = \frac{RIA_{uncharged} - RIA_{charged}}{RIA_{uncharged}} \times 100\% \quad (6)$$

where EL is the total elongation, RIA is the reduction in area, and the subscript loss, uncharged, and charged represent the plasticity loss, the specimens without hydrogen charging, and the specimens with hydrogen charging, respectively.

Microhardness and Microstructural Characterization

The hardness and the distribution of welding joints have great influences on the properties of welding joints. This study measured the hardness in the region of welding joints and parts of adjacent BM after multi-pass welding. Meanwhile, the contour maps of hardness distribution were drawn according to the hardness test results. Since the welding joints in this study are symmetrical along the thickness and weld direction, only a quarter of the welding joint was tested every 0.5 mm along the horizontal and vertical direction. Hardness tests were carried out using Vickers hardness by a 500 g load.

The different regions of welding joints, such as WM, fusion line (FL), CGHAZ, and FGHAZ, were observed using an optical microscope (OM, Leica DMIRM), and the metallographic specimens of welding joints were etched in a 4% Nital solution for 20 s. A transmission electron microscope (TEM, FEI Tecnai G2 F20) was used to understand the delicate microstructures of WM and HAZ, and the TEM specimens were twin-jet polished in a solution

containing 6 vol% perchloric acid alcohol solution at 27 V and -20°C . Electron backscattering diffraction (EBSD, FE-SEM ZEISS ULTRA 55) is used to confirm the RA content in HAZ. The EBSD specimens were electro-polished in 6% perchloric acid alcohol solution at 15 v for 16 s.

RESULTS

Microstructures of Welding Joints

Figure 1a and d shows the microstructures of WM A and WM B, which are composed of acicular ferrite. CGHAZ of two welding joints is all composed of lath martensite, and the prior austenite grain size of welded joint B (WJB) is a little larger than welded joint A (WJA) (Fig. 1b and e). As shown in Fig. 1c and f, the FGHAZ of two welding joints comprises lath martensite. The difference in grain sizes of the

two weld joints is mainly due to the addition of Ti to WJA, which can refine the grains. Figure 1g and h shows the detail of the FL of WJA and WJB. FL contains lath martensite and acicular ferrite, which are only about $20\text{--}30\ \mu\text{m}$ wide.

Ti mainly regulates the microstructure and properties of steel through grain refinement (TiN) and precipitation strengthening (TiC) in steel.⁴⁴ The morphology of TiN precipitated at high temperature is cubic, while TiC precipitated at low temperature is very small spherical. Figure 2 shows the representative TEM microstructure of WM A, CGHAZ A, WM B, CGHAZ B, and the magnified TiN and TiC precipitates in WJA. As Fig. 2a and c shows, some TiN and TiC precipitates appear in WM A, and TiC almost disappears after the welding process (Fig. 2b and d). This is because the precipitation and existence temperature of TiN exceeds 1300°C .⁴⁵

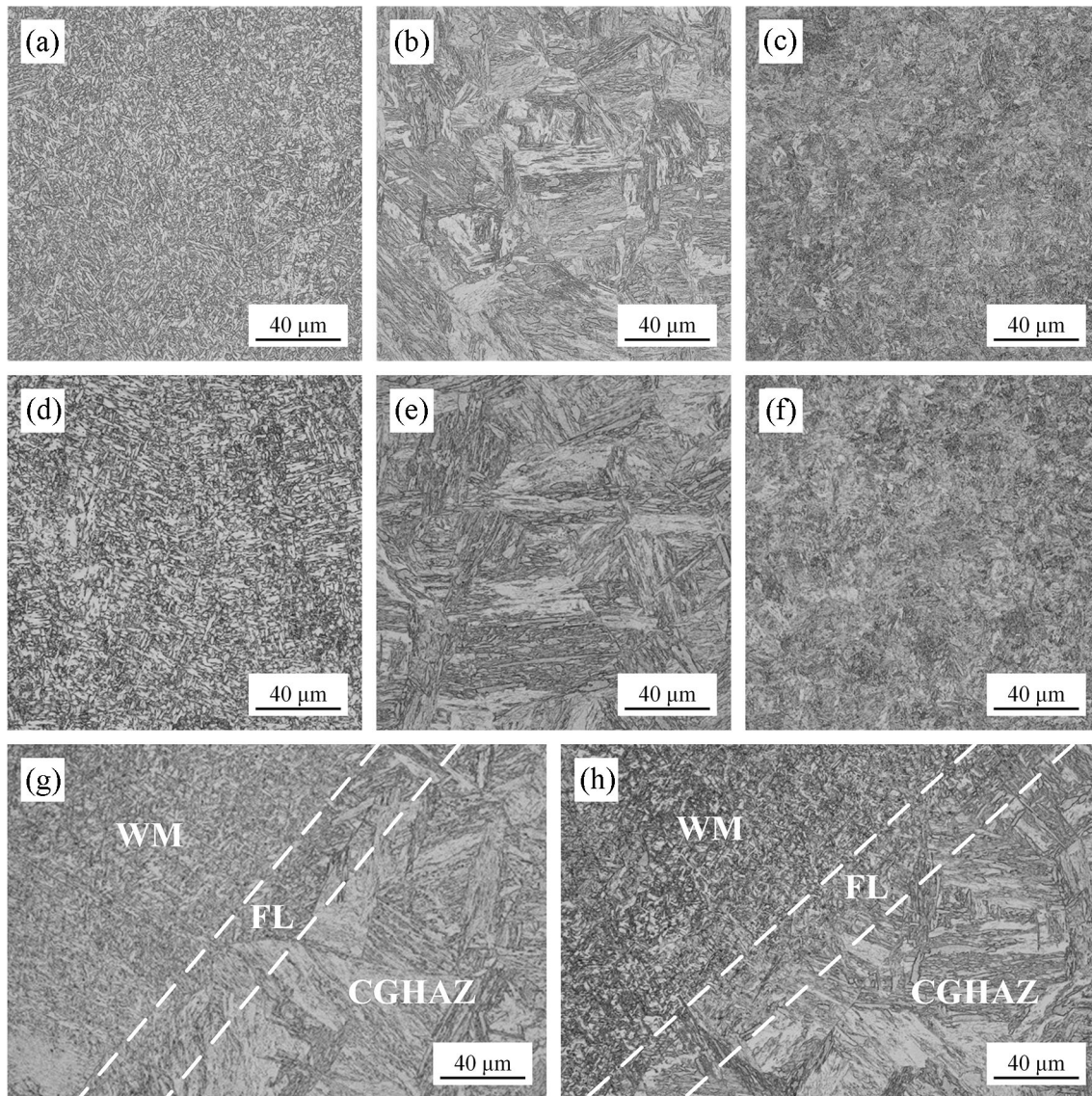


Fig. 1. Optical micrographs of different regions of different weld joints. (a) WM A, (b) CGHAZ A, (c) FGHAZ A, (d) WM B, (e) CGHAZ B, (f) FGHAZ B, (g) FL A, (h) FL B.

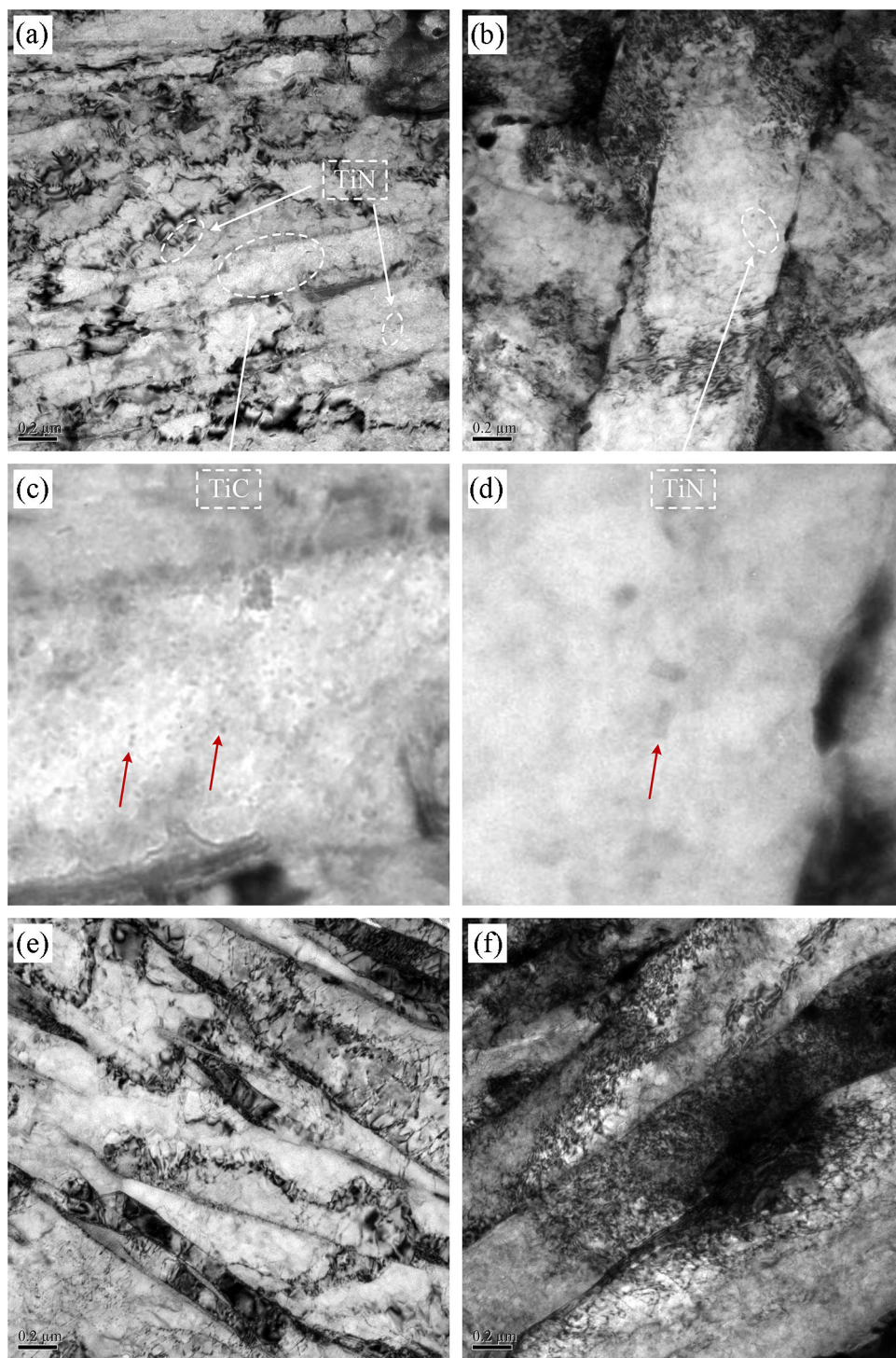


Fig. 2. TEM micrographs of different regions of two welding joints. (a) WM A, (b) CGHAZ A, (c) magnified TiC, (d) magnified TiN, (e) WM B, (f) CGHAZ B.

The microstructure of CGHAZ of two welding joints was composed of coarse martensite lath with high dislocation density (Fig. 2b and f). The martensite lath width of CGHAZ (0.5–1 μm) was much wider than WM (200–300 nm).

Supplementary Fig. S3 shows the representative band contrast and phase images of HAZ A (a) and HAZ B (b). RA is a critical phase for medium manganese steel to increase strength and toughness, and it is very significant whether there is RA in the heat-affected zone. Supplementary Fig. S3

shows that there is almost no RA in both HAZ A and HAZ B, indicating that HAZ is only composed of martensite.

Hydrogen Permeation Behavior of the Welding Joints

As shown in Fig. 3, the hydrogen permeation oxidation current of two welding joints rises rapidly after penetrating through the specimens. There is also an apparent phenomenon in which the oxidation current of WJB is always larger than WJA, which suggests that the hydrogen permeation resistance of WJA is greater than that of WJB. Figure 3 also shows that the curves can be divided into two stages after penetrating through the specimens, where the curve of WJB decreases a bit after reaching the highest point and then stays steady. Still, the curve of WJA rises linearly and slowly after rising rapidly for a certain period. Finally, the hydrogen permeation oxidation current of the two welding joints is almost the same.

Some important permeation parameters of the two welding joints are listed in supplementary Table SII. Here, the values of I_{ss} and t_{lag} are directly obtained from Fig. 3, and J_{ss} , D_{eff} , C_{0R} , and N_T are calculated by Eqs. 3, 4, 5 and 6. Supplementary Table SII shows that t_{lag} of WJA and WJB is 17.9 min and 14.7 min, respectively, and I_{ss} WJA and WJB is 3.93×10^{-5} A (the highest point at about 30 min) and 4.14×10^{-5} A (the highest point at 120 min). D_{eff} of WJA and WJB was $1.55 \times 10^{-10} \text{ m}^2 \text{ s}^{-1}$ and $1.89 \times 10^{-10} \text{ m}^2 \text{ s}^{-1}$, which means hydrogen atoms in WJB diffuse faster than WJA. Furthermore, the number of hydrogen traps of WJB is less than WJA, which can also be obtained from N_T .

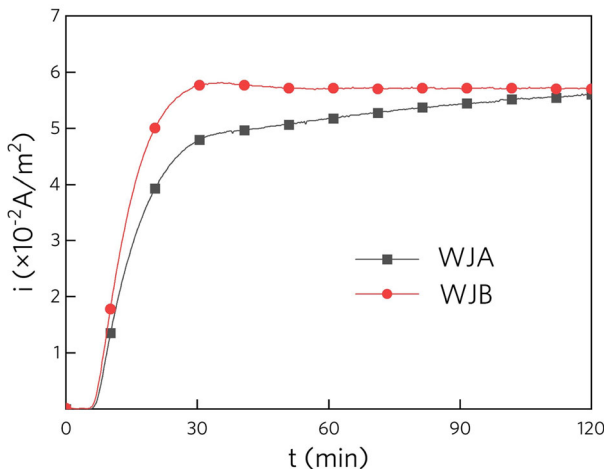


Fig. 3. Hydrogen permeation oxidation current density curve of different welding joints.

Hydrogen Concentration of WM and HAZ After Hydrogen Charging

Figure 4 shows the hydrogen concentration of WM and HAZ after hydrogen charging for 1 h, 2 h, and 1 h with exposure to air for 60 h, where Fig. 4a is that of HAZ. Overall, the hydrogen concentration of WJA is larger than for WJB for all hydrogen charging conditions, whether WM or HAZ. The hydrogen concentration of HAZ is higher than that of WM after hydrogen charging for both 1 h and 2 h because HAZ contains a high density of dislocations, which can trap many hydrogen atoms. Besides, the hydrogen concentration in WM A after hydrogen charging for 1 h and exposure to air for 60 h is much larger than that of WM B. However, the hydrogen concentration in HAZ of two welding joints under the same hydrogen charging condition is almost identical. This phenomenon is because some TiC exists in WM A, but WM B does not. Compared with the specimen after being exposed to air for 60 h, it can be considered that most of the hydrogen atoms in the specimens are indiffusible hydrogen atoms at room temperature. So, it can be inferred that hydrogen concentration differences between charged and exposed specimens are diffusible hydrogen concentrations, as listed in Table II.

Table II lists the diffusible hydrogen concentration of WM and HAZ of different welding joints. The diffusible hydrogen concentration of HAZ is much larger than for WM for all specimens because there are many dislocations in HAZ, which are regarded as reversible hydrogen traps. Meanwhile, the diffusible hydrogen concentration in WM A is smaller than in WM B, but the diffusible hydrogen concentration in HAZ A is larger than in HAZ B under the same hydrogen charging condition because WM A contains more TiC. The reason why the diffusible hydrogen concentration in HAZ A is larger than in HAZ B would be that the primary austenite grain in HAZ A is finer than in HAZ B because of the addition of Ti.

Slow Strain Rate Tensile Properties and Fractography of the Welding Joints

Figure 5 is the engineering stress-strain curves and shows that the ELs of WJA are lower than that of WJB under all conditions. Figure 5 shows that WJA-2 h fractured at the elastic stage. Figure 6 shows the total elongation, and the reduction in the area of two welding joints with different hydrogen charging times. Because the strength of the welded joint is higher than that of BM, the deformation is mainly concentrated in BM. Combined with EBSD results, we can say that the uniform elongation enhanced by RA through the TRIP effect mainly occurs in BM. Figure 6 shows that the EL of uncharged WJA is 13.2% and uncharged WJB is 19.8%, which is 6.6% more than in uncharged WJA. Besides, the EL of WJA with hydrogen charging for

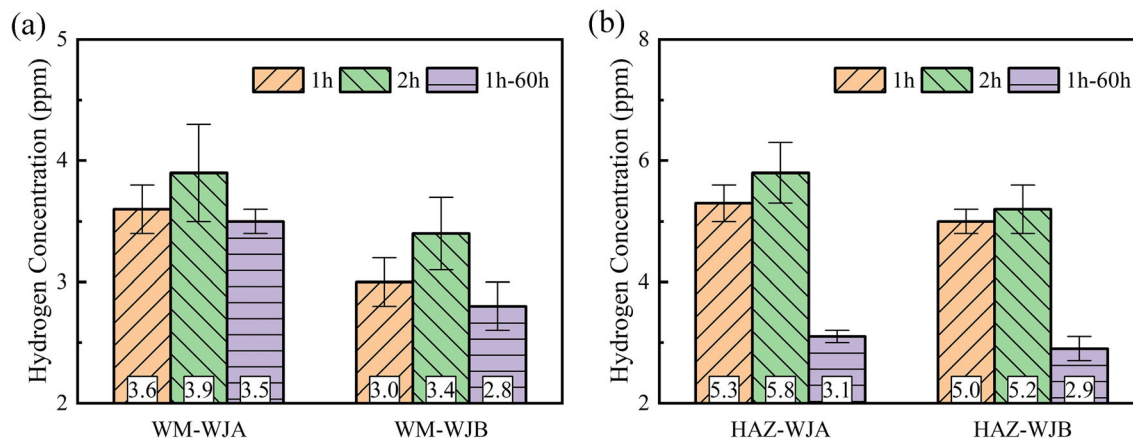


Fig. 4. Hydrogen concentration after different hydrogen charging times. (a) WM; (b) HAZ.

Table II. Diffusible hydrogen concentration of WM and HAZ of different welding joints

Hydrogen charging time		Diffusible hydrogen concentration (ppm)	
		WM	HAZ
WJA	1 h	0.2 ± 0.1	2.2 ± 0.5
	2 h	0.4 ± 0.1	2.7 ± 0.6
WJB	1 h	0.2 ± 0.1	2.1 ± 0.1
	2 h	0.6 ± 0.4	2.3 ± 0.2

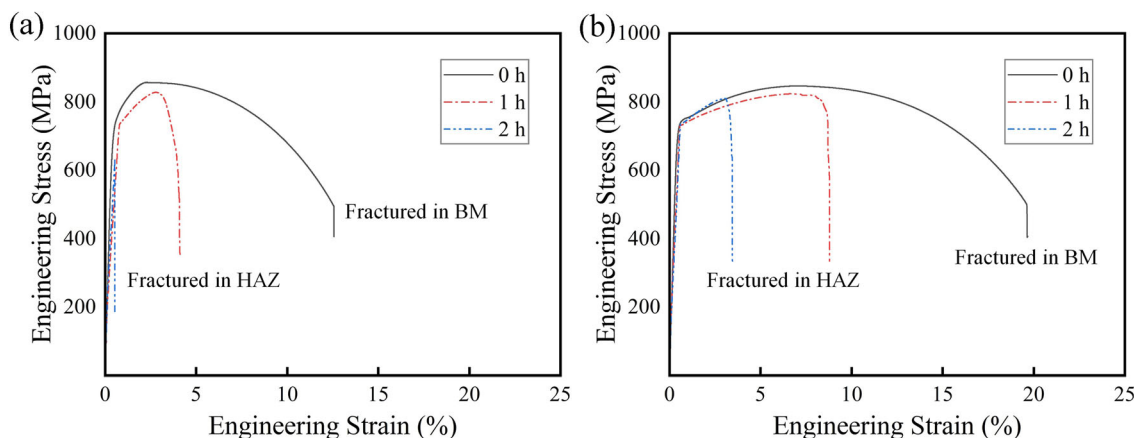


Fig. 5. Engineering stress–strain curves of different welded joints with different hydrogen charging. (a) WJA, (b) WJB.

2 h decreased to 0% and WJB remained at 3.9%. Furthermore, the RIA of uncharged WJA is 68.8%, which is almost the same as WJB, and the RIA of the WJA with 2 h hydrogen charging decreases to 0%, but WJB remains at 5.3%. Another obvious phenomenon shown in Fig. 6 is that EL linearly decreases, but RIA exponentially decreases with hydrogen charging time.

Table III lists the loss of EL and RIA of different welding joints with different hydrogen charging times. The effect of microstructures and residual stress should be the main influences on the difference in failure regime between two welding joints.

The EL_{loss} of WJA with hydrogen charging for 1 h is 59.1%, which is about two-thirds of hydrogen charging for 2 h, and similar trends have also occurred in WJB. RIA_{loss} of WJA with hydrogen charging for 2 h is 100%, which is 10% more than that with hydrogen charging for 1 h, and similar trends have also occurred in WJB. Another obvious phenomenon shown in Table III is that the loss percents of WJA with different hydrogen charging times are all larger than WJB, which means the HE susceptibility of WJA is larger than WJB.

Observation of the fracture profile is shown in Fig. 7a and b. Different from the specimens without

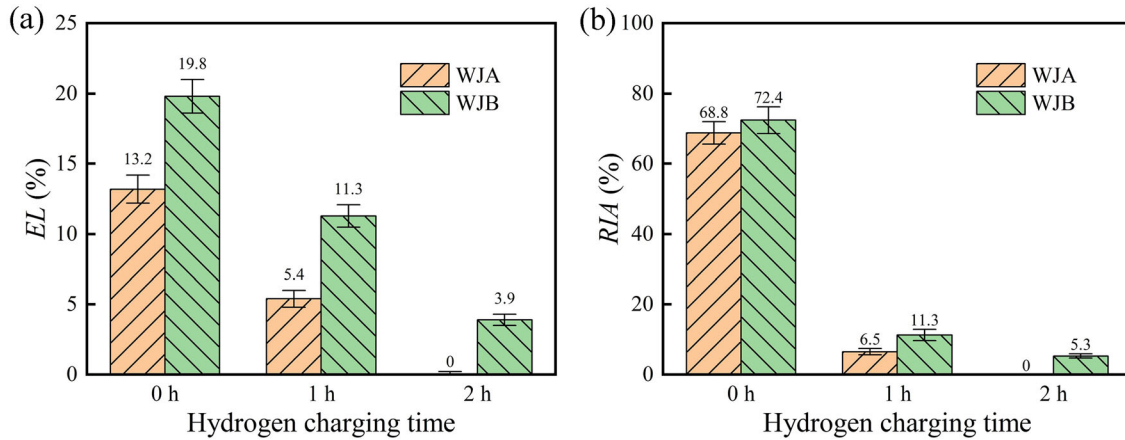


Fig. 6. Total elongation (a) and reduction in area (b) of different welding joints with different hydrogen charging times.

Table III. Embrittlement indexes of different welding joints

Hydrogen charging time	WJA		WJB	
	1 h	2 h	1 h	2 h
EL _{loss} (%)	59.1	100	42.9	80.3
RIA _{loss} (%)	90.6	100	84.4	92.7

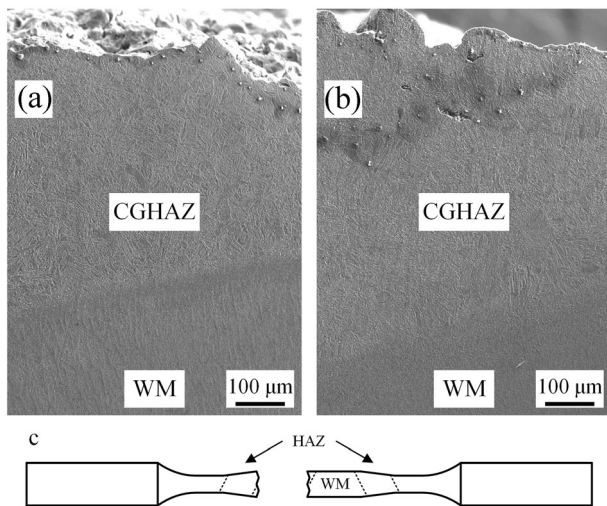


Fig. 7. Fracture profile and schematic diagram of fracture position of welding joint. (a) WJA-2h, (b) WJB-2h, (c) schematic diagram.

hydrogen charging fractured at BM, the specimens with hydrogen charging were fractured at WM and CGHAZ, and the fracture surface is perpendicular to the axis of the specimen. The schematic diagram of the fracture location is shown in Fig. 7c.

Figure 8 shows the fractography of tensile specimens of two welding joints. The macro-fractography (Fig. 8a, d, g and j) was divided into two regions (A and B) for all the specimens, where region A is WM and region B is HZA. Region A of WJA with hydrogen charging for 1 h (Fig. 8b) consists of small dimples

and some microcracks, and region B (Fig. 8c) consists of quasi-cleavage and lots of microcracks. Compared with hydrogen charging for 1 h, WJA with hydrogen charging for 2 h consists of quasi-cleavage (region A) and intergranular fracture (region B). This is because hydrogen atoms reduce the binding force of closely packed plane atoms. Besides, there are some small cracks perpendicular to the main crack in the fracture. The cracks are secondary cracks caused by the triaxial stress state and local stress concentration due to the aggregation of hydrogen atoms. When hydrogen charging time increases, the grain boundaries of HAZ are damaged seriously. Therefore, the fracture mode of HAZ of WJA was intergranular, and the WM with low HE susceptibility fracture mode is cleavage. However, WJB with hydrogen charging for 1 h consists of big and small dimples. Region A of WJB with hydrogen charging for 2 h (Fig. 8k) consists of quasi-cleavage (region A) and some dimples, and Region B (Fig. 8l) consists of trans-granular and some microcracks (region B). Compared with WJA, the intergranular fracture does not appear at HAZ of WJB, and there are still many dimples in WM. Additionally, comparing this macro-fractography of two welding joints (Fig. 8a, d, g and j), a delamination phenomenon that stratified cracks appeared in the WJB. The pictures show that the HAZ of WJA is more brittle than WJB, and the WM of WJA is also more brittle than WJB under the same hydrogen charging conditions. Overall, this fracture morphology indicates that the HE susceptibility of WJB is lower than WJA.

Hardness Distribution

Figure 9 shows the hardness distribution and tested region of the two welding joints, including WM, HAZ, and BM. Figure 9a and b shows the tested regions of WJA and WJB, and Fig. 9c and d shows the corresponding contour map of the hardness distribution, respectively. Figure 9 also shows that the WM average hardness of WJA was higher than that of WJB, because WM A has a higher C

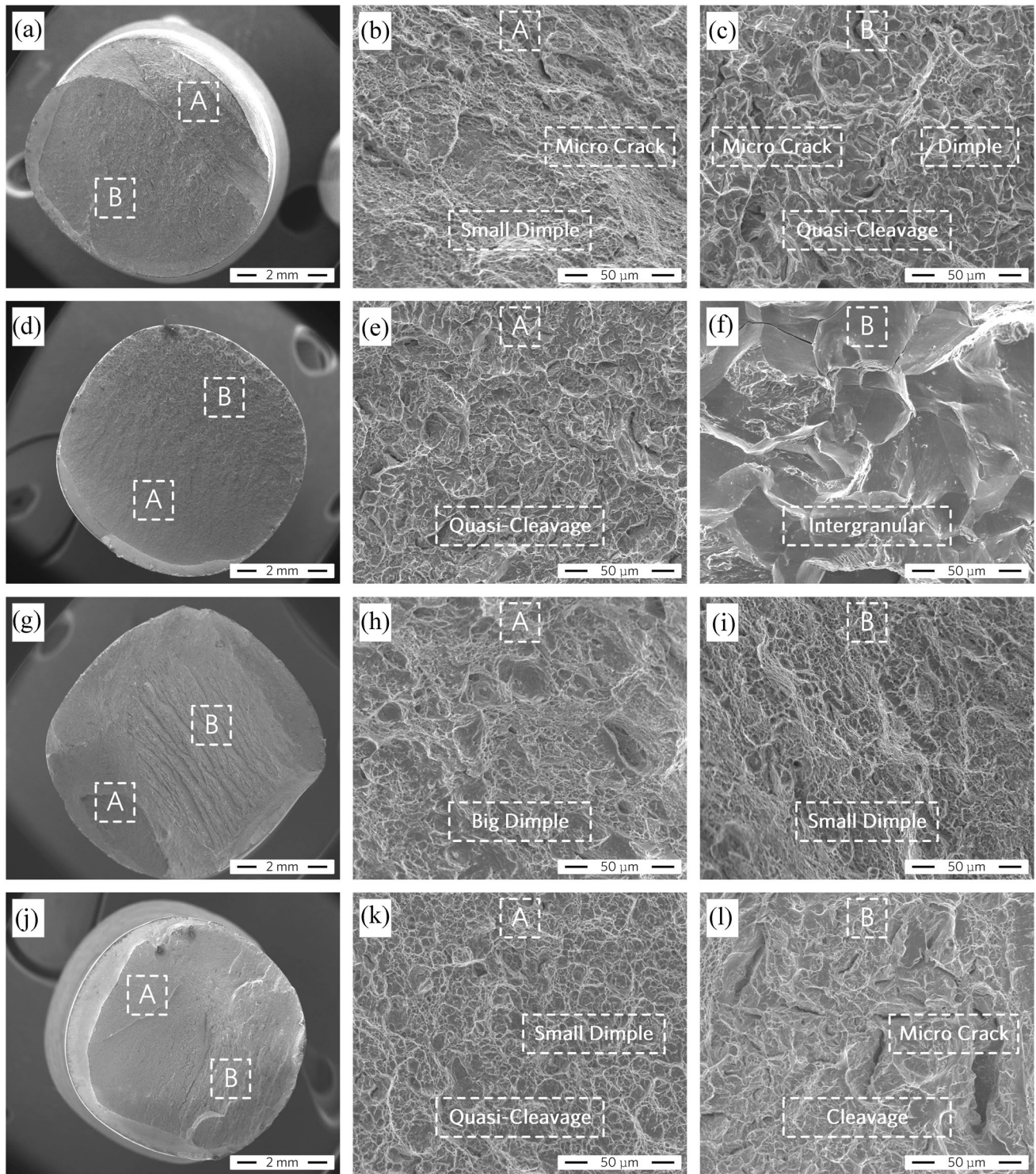


Fig. 8. Fractography of the slow strain rate tensile specimens with different hydrogen charging times. (a, b, and c) WJA with 1 h hydrogen charging. (d, e, and f) WJA with 2 h hydrogen charging. (g, h, and i) WJB with 1 h hydrogen charging. (j, k, and l) WJB with 2 h hydrogen charging.

content and added small amount of Ti compared with WM B, although the microstructures of two WMs are all acicular ferrite. However, the FGHAZ average hardness of WJA was lower than that of WJB, especially at the welding pass near the

surface. This phenomenon is because the contents of Mn in BM B are larger than that in BM A. The hardness of the martensite in the FGHAZ will be significantly increased with the Mn content. The maximum hardness of WJA is about 405 HV500,

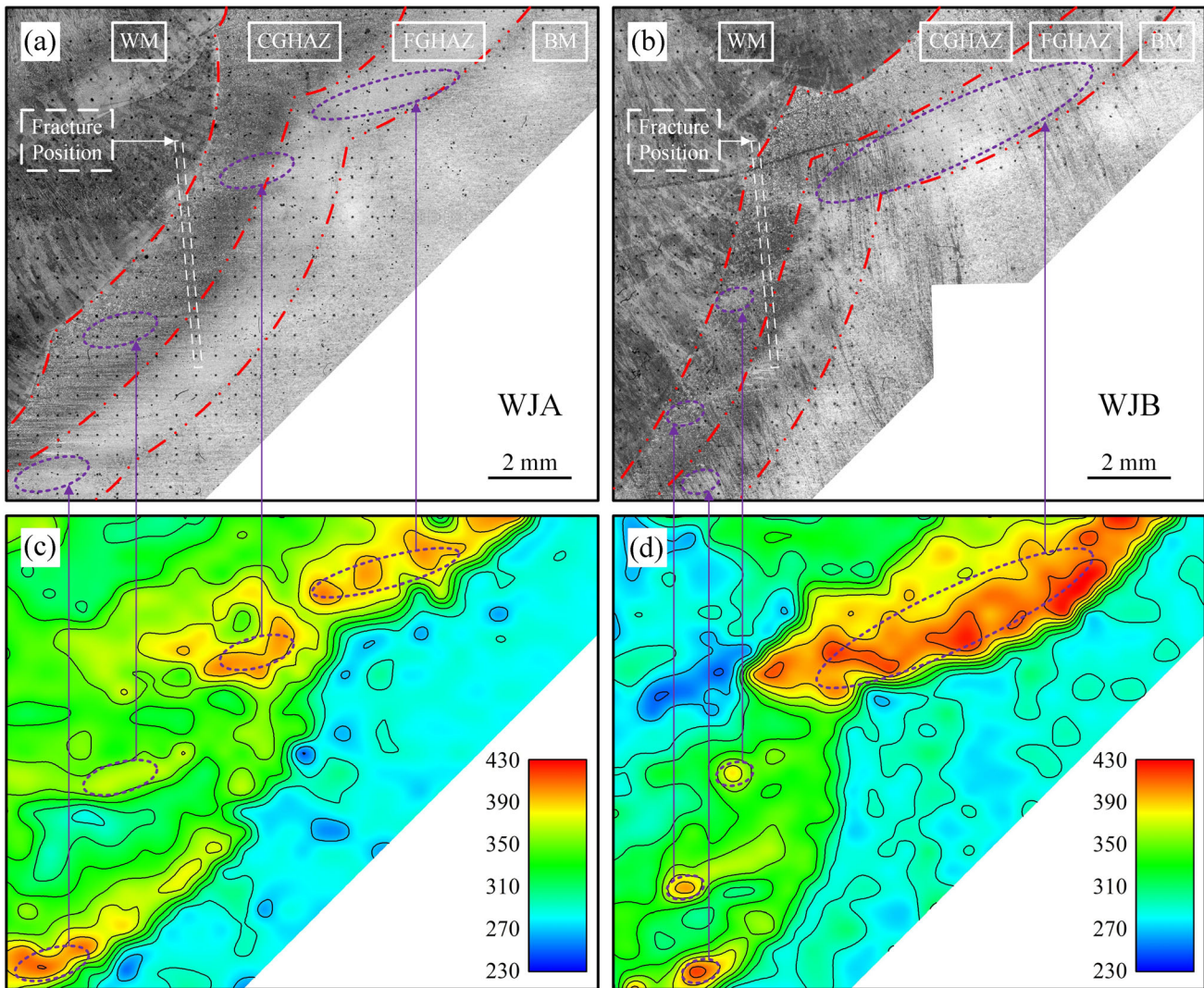


Fig. 9. Hardness distribution of WJA (a, c) and WJB (b, d).

which appears at the center and near the surface. The maximum hardness of WJB is about 425 HV500, which is larger than WJA and appears at the center and near the surface. Each welding pass will give rise to a high hardness area, which appears near each fusion line of each pass (FGHAZ). There are two reasons for this phenomenon: the low base metal temperature leads to a large cooling rate in the first welding pass, which increases the dislocation density of martensite, and the other is the subsequent welding passes provide different tempering times. The welded joints are tempered once at the center of the steel plates, twice at the quarter of the steel plates, and not tempered at the edge of the steel plates. The hardnesses of BM of two welded joints are almost the same, because the 630°C intercritical annealing heat treatment reduces the dislocation density in the martensite and introduces some RA.

DISCUSSION

Fracture Behaviors of Medium Manganese Steel Welding Joints with Hydrogen Charging

In this study, the microstructures of two welding joints are acicular ferrite (WM), martensite (HAZ), and tempered martensite with RA (BM). In the standard tensile tests of welding joints, namely without hydrogen charging, the fracture position usually appears in BM, whose strength is the lowest. This phenomenon is because plastic deformation first occurs in the region of low strength (BM). With the increase in work hardening effect, plastic deformation begins in the region that will not deform before. However, the fracture position of the specimens after hydrogen charging in the present study was not located at the region of maximum plastic deformation (BM). The fracture occurs near the welding joint center where the

plastic deformation is small, as presented in Fig. 7. The fracture surface, which includes CGHAZ and WM, is perpendicular to the axis of the specimen and crosses over FL. WM hardly deforms, and BM deforms the most during tensile, but the fracture position is in the transition region of deformation and close to the WM side.

It is widely accepted that HE mechanisms of welding joints are the HELP and stress intensity model. Beechem proposed a model of stress field intensity and fracture behavior at the crack tip and hydrogen concentration.⁴⁶ The fracture mode is intergranular fracture when the stress field strength factor is low, and hydrogen concentration is high. Contrarily, when the stress field intensity factor is high and the hydrogen concentration is low, the fracture modes are quasi-cleavage and microvoid aggregation fractures. The stress state in this region is very complex, and the stress field intensity factor is also large because some additional internal stress will be produced because of the inhomogeneous deformation. Moreover, the original internal stress in this region is also large, which will make the HE susceptibility of welding joints larger. From the viewpoint of microstructures, the coarse martensite in CGHAZ also has high HE susceptibility. Furthermore, from the fractography of tensile specimens with hydrogen charging (Fig. 8), there is a lot of cleavage fracture in CGHAZ of WJA after hydrogen charging for 1 h, while the WM region is composed of small dimples. However, there is no obvious cleavage in CGHAZ of WJB, but the dimple is small and shallow.

This suggests that cracks first form and propagate at CGHAZ, then pass through FL and enter WM, and finally lead to the fracture of the whole specimen. Furthermore, the fractography of CGHAZ and WM of WJA with hydrogen charging for 2 h is intergranular and cleavage, respectively. CGHAZ of WJB is a cleavage fracture, and some cleavage also appeared in WM, which indicates that the cracks also form in CGHAZ, propagate into WM, and finally fracture. It is widely known that hydrogen atoms can reduce the binding force between atoms, and the critical fracture stress of different microstructures is different under different environments. This phenomenon is because the critical fracture stress of CGHAZ is reduced after hydrogen charging. In summary, there are two phenomena in this research. One is that the fracture position occurs at HAZ because of its immense stress and high hydrogen concentration, and the other is that HE susceptibility of WJA is larger than WJB. This can also explain why the fracture does not occur where the deformation is the largest but at CGHAZ and WM.

Influences of Chemical Compositions on HE of Welding Joints

HE susceptibilities of the two studied welding joints are very different because of the differences in the compositions of steels. In this study, there are two main differences in the chemical composition of two welding joints. From the results of hydrogen concentration, the hydrogen concentration of WJA is larger than that of WJB because about 0.03% Ti added in WJA causes some TiC precipitates to be present in WM. Ti can increase hydrogen concentration after hydrogen charging. Ti has a strong binding force with hydrogen atoms. The same results of the hydrogen trap number in WJA are much larger than those in WJB and were also obtained at hydrogen permeation experiments, and the calculation results are based on the curve (supplementary Table SII). So, it can be inferred that TiC increases the total hydrogen concentration of WM, therefore increasing HE susceptibility. The results show that the hydrogen concentration of HAZ is much greater than that of WM, and HE susceptibility is also much larger. On the other hand, the microstructures of HAZ of WJA are similar to WJB, which means the CGHAZ properties of two welding joints should be the same, but the HE susceptibility of two welding joints is quite different. It is well known that adding Ti and grain refinement will increase the hydrogen concentration in steel. Meanwhile, the total hydrogen concentration or diffusible hydrogen concentration in HAZ of WJA is larger than in WJB under the same hydrogen charging condition because of the strong binding force between Ti and hydrogen atoms and the grain refinement effect introduced by TiN. The HAZ fractography of WJA changes from quasi-cleavage to intergranular when diffusible hydrogen increases from 2.2 ppm to 2.7 ppm. This means a critical diffusible hydrogen concentration value between 2.2 ppm and 2.7 ppm will change the fracture mode of HAZ of WJA.

From the discussion above, it can be concluded that Ti can increase HE susceptibility in WM or HAZ. However, a small amount of Ti added to WM is generally used to improve the weldability of low alloy steels and also needs to be added to medium manganese steels to avoid the austenite grain growth during the heating process, thus improving the strength and toughness. The traditional evaluation of the effect of Ti on the weldability of steel is not suitable for the situation considering hydrogen. Therefore, the Ti content in BM and WM of medium manganese steels should be controlled within a reasonable range based on the premise that HE, weldability, strength, and toughness are fully considered.

Different chemical compositions will also lead to different hardness distributions. The maximum hardness and the difference in hardness will affect the quality of welded joints, though the existing results are obtained through experience. The maximum hardness and hardness difference of Joint B are greater than those of Joint A, but HE susceptibility is lower than that of Joint A. It shows that maximum hardness and hardness differences are not the main influences on HE. Therefore, these influences do not apply to the welding joint of medium manganese steel containing some RA after hydrogen charging. Another significant issue is that the Mn content of the BM of WJA is 4.38%, which is very different from WJB (5.45%). However, the effect of manganese content in medium manganese steel on the HE susceptibility of welding joints is not known clearly, and further studies are needed to investigate the relationship between HE susceptibility and Mn content. The main toughening mechanism is the austenite transformation-induced plasticity effect, formed during inter-critical annealing after quenching. In addition, some studies have shown that improving the stability of austenite is also helpful in improving the resistance of HE susceptibility.¹²⁻¹⁴ However, obtaining enough stable austenite in welding joints is complicated through ordinary methods. Therefore, it is necessary to investigate a new method to improve the HE resistance of medium manganese steel welding joints by obtaining stable austenite.

HE Mechanisms of WM and HAZ of Welded Joints

HE mainly affects weld quality in the actual weld, and hydrogen atoms first form in WM and then enter HAZ, which comes from vapor, oil, and combustion products of electrode coating during the welding process. However, HE also affects structural safety in the service environment containing hydrogen, mainly from the marine environment, corrosion, and cathodic protection. From the viewpoint of the HE mechanism, the principles that hydrogen concentration and microstructures affect HE are suitable for the two situations. As described in the results above, the tensile specimens initially crack at HAZ after hydrogen charging, indicating that HAZ has significant HE susceptibility.

For the specimen of WJA after hydrogen charging for 1 h, the fractography of WM is composed of small shallow dimples and some large flat cleavage-like regions. This shows that plastic deformation occurs in many places but will not have been fully developed before the specimen fracture. Hydrogen first promotes local plastic deformation according to the HELP mechanism. However, the total hydrogen concentration is high because of the existence of TiC, and some flat surfaces were formed under the HEDE mechanism. Finally, the specimen fractured under the combined action of the HELP and HEDE

mechanisms. Compared with WM, the fractography of HAZ is quasi-cleavage. This is because the microstructure of HAZ is martensite with high-density dislocations, resulting in high hydrogen concentration. Hydrogen atoms are segregated along the closely packed surface of martensite, weakening the binding force between atoms and leading to quasi-cleavage fracture as per the HEDE mechanism. When the hydrogen charging time is extended to 2 h, which means diffusible hydrogen concentration increases, the fractography of WM changes from small dimples to quasi-cleavage and cleavage. Like in WM, the fractography of HAZ changes from quasi-cleavage to intergranular because of the increase of diffusible hydrogen concentration; this is further attributed to those hydrogen atoms reducing the atomic binding force between the closely packed surface and grain boundaries owing to the HEDE mechanism.

For the specimen of WJB after hydrogen charging for 1 h, the fractography of WM is composed of big and small dimples, where the large dimples represent sufficient plastic deformation and the small dimples represent insufficient plastic deformation. Compared with WM, the fractography of HAZ is composed of small shallow dimples, which indicates the fracture mechanism of this specimen is HELP. When the hydrogen charging time is extended to 2 h, the fractography of WM changes from big dimples (HELP) to small dimples and quasi-cleavage (HELP and HEDE), and the fractography of HAZ changes from small dimples (HELP) to cleavage (HEDE). In summary, the HE susceptibility of WJB is smaller than in WJA.

CONCLUSION

In this study, the effects of chemical composition, microstructure, and different hydrogen charging times on the HE behavior of two low-carbon medium manganese steel welding joints were studied using a slow strain rate tensile experiment, hydrogen permeation experiment, and melt extraction experiment. We obtained the following conclusions based on the experimental results:

1. In the standard tensile test of welding joints, the fracture position usually appears in BM. However, the fracture position becomes HAZ after hydrogen charging. The crack started at HAZ because of the high hydrogen embrittlement susceptibility of martensite with coarse grain size.
2. Hydrogen concentration of welding joint A (WJA) is larger than in welding joint B (WJB), and the hydrogen concentration of HAZ is higher than that of WM after all hydrogen charging conditions. Besides, the diffusible hydrogen concentration of HAZ is much larger than WM for all specimens.
3. The microstructures of WJA and WJB are

similar, but the HE susceptibility of WJA is larger than that of WJB. Because of the absence of RA in HAZ, HE susceptibility is mainly attributed to the hydrogen concentration in HAZ, which is mainly affected by the Ti content.

4. When the hydrogen charging time of WJA increases from 1 h to 2 h, the fractography of WM changes from small shallow dimples (HELP) to quasi-cleavage and cleavage (HEDE), and the fractography of HAZ changes from quasi-cleavage (HEDE) to intergranular (HEDE).
5. When the hydrogen charging time of WJB increases from 1 h to 2 h, the fractography of WM changes from big dimples and small dimples to small dimples and quasi-cleavage, and the fractography of HAZ changes from small dimples to cleavage.

SUPPLEMENTARY INFORMATION

The online version contains supplementary material available at <https://doi.org/10.1007/s11837-023-06064-2>.

ACKNOWLEDGEMENTS

The authors gratefully appreciate the financial support from the National Natural Science Foundation of China (No. 51975391) and the National High-tech R&D Program (863 Program) (No. 2015AA03A501).

CONFLICT OF INTEREST

The authors declare that they have no known competing financial interests or personal relationships that could have appeared to influence the work reported in this paper.

REFERENCES

1. X.K. Jin, L. Xu, W.C. Yu, K.F. Yao, J. Shi, and M.Q. Wang, *Corros. Sci.* 170, 108421 (2020).
2. L. Chen, X.L. Xiong, X. Tao, Y.J. Su, and L.J. Qiao, *Corros. Sci.* 166, 108428 (2020).
3. T. Das, S.V. Brahim, J. Song, and S. Yue, *Corros. Sci.* 190, 109701 (2021).
4. X.Y. Cheng and H.X. Zhang, *Corros. Sci.* 174, 108800 (2020).
5. M. Dadfarnia, P. Novak, D.C. Ahn, J.B. Liu, P. Sofronis, D.D. Johnson, and I.M. Robertson, *Adv. Mater.* 22, 1128 (2010).
6. J. Song and W.A. Curtin, *Acta Mater.* 59, 1557 (2011).
7. J. Song and W.A. Curtin, *Nat. Mater.* 12, 145 (2013).
8. J. Song and W.A. Curtin, *Acta Mater.* 68, 61 (2014).
9. R.A. Oriani and P.H. Josephic, *Acta Metall.* 25, 979 (1977).
10. J.F. Lessar and W.W. Gerberich, *Metall. Trans. A* 7, 953 (1976).
11. S.P. Lynch, *Acta Metall.* 36, 2639 (1988).
12. Z. Tarzimgohadam, M. Rohwerder, S.V. Merzlikin, A. Bashir, L. Yedra, S. Eswara, D. Ponge, and D. Raabe, *Acta Mater.* 109, 69 (2016).
13. Y. Chen, D. Haley, S.S.A. Gerstl, A.J. London, F. Sweeney, R.A. Wepf, W.M. Rainforth, P.A.J. Bagot, and M.P. Moody, *Science* 355, 1196 (2017).
14. J.M. Cairney and H.Z. Lu, *Science* 367, 171 (2020).
15. J. Zhao and Z. Jiang, *Prog. Mater. Sci.* 94, 174 (2018).
16. D.Z. Zhang, X.H. Gao, L.X. Du, Y. Du, H. Wang, Z.G. Liu, and G.Q. Su, *Mater. Sci. Eng. A* 765, 138278 (2019).
17. M.A. Mohtadi-Bonab, J.A. Szpunar, and S.S. Razavi-Tousi, *Int. J. Hydrogen Energ.* 38, 13831 (2013).
18. D. Wang, X. Lu, Y. Deng, X. Guo, and A. Barnoush, *Acta Mater.* 166, 618 (2019).
19. H. Liu, L.X. Du, J. Hu, H.Y. Wu, X.H. Gao, and R.D.K. Misra, *J. Alloys Compd.* 695, 2072 (2017).
20. J. Hu, L.X. Du, W. Xu, J.H. Zhai, Y. Dong, Y.J. Liu, and R.D.K. Misra, *Mater. Charact.* 136, 20 (2018).
21. J. Hu, L.X. Du, G.S. Sun, H. Xie, and R.D.K. Misra, *Scr. Mater.* 104, 87 (2015).
22. X.Y. Qi, L.X. Du, J. Hu, and R.D.K. Misra, *Mater. Sci. Eng. A* 718, 471 (2018).
23. L.Y. Lan, M. Yu, and C.L. Qiu, *Mater. Sci. Eng. A* 742, 442 (2019).
24. J.L. Yang, F. Huang, Z.H. Guo, Y. Rong, and N. Chen, *Mater. Sci. Eng. A* 665, 76 (2016).
25. X. Zhu, W. Li, H.S. Zhao, and X.J. Jin, *Int. J. Hydrogen Energ.* 38, 10694 (2013).
26. X. Zhu, W. Li, H. Zhao, L. Wang, and X. Jin, *Int. J. Hydrogen Energ.* 39, 13031 (2014).
27. A.E. Pontini and J.D. Hermida, *Scripta Mater.* 37, 1831 (1997).
28. T. Michler, C. San Marchi, J. Naumann, S. Weber, and M. Martin, *Int. J. Hydrogen Energ.* 37, 16231 (2012).
29. Y. Du, X.H. Gao, L.Y. Lan, X.Y. Qi, H.Y. Wu, L.X. Du, and R.D.K. Misra, *Int. J. Hydrogen Energ.* 44, 32292 (2019).
30. Y. Du, X.H. Gao, Z.W. Du, L.Y. Lan, X.Y. Qi, R.D.K. Misra, H.Y. Wu, and L.X. Du, *Int. J. Hydrogen Energ.* 46, 8269 (2021).
31. X.Y. Qi, L.X. Du, J. Hu, and R.D.K. Misra, *Steel Res. Int.* 89, 1700422 (2018).
32. J.H. Yoo, K.T. Han, Y.H. Park, and C.H. Lee, *Mater. Chem. Phys.* 146, 175 (2014).
33. T.M. Zhang, W.M. Zhao, Q.S. Deng, W. Jiang, Y.L. Wang, Y. Wang, and W.C. Jiang, *Int. J. Hydrogen Energ.* 42, 25102 (2017).
34. S.J. Kim, H.G. Jung, and K.Y. Kim, *Scripta Mater.* 67, 895 (2012).
35. E. López Martínez, H.J. Vergara Hernández, O. Flores, and B. Campillo, *Hydrogen ISIJ Int.* 55, 2435 (2015).
36. L.Y. Lan, X.W. Kong, Z.Y. Hu, C.L. Qiu, D.W. Zhao, and L.X. Du, *Corros. Sci.* 112, 180 (2016).
37. Z.H. Fu, T. Li, M.L. Shan, G.Q. Gou, Z.Y. Zhu, C.P. Ma, W. Gao, and Y.C. Hu, *Corros. Sci.* 148, 272 (2019).
38. Y.H. Fan, B. Zhang, H.L. Yi, G.S. Hao, Y.Y. Sun, J.Q. Wang, E.H. Han, and W. Ke, *Acta Mater.* 139, 188 (2017).
39. T. Hojo, E. Akiyama, H. Saitoh, A. Shiro, R. Yasuda, T. Shobu, J. Kinugasa, and F. Yuse, *Corros. Sci.* 177, 108957 (2020).
40. H.Y. Tian, J.C. Xin, Y. Li, X. Wang, and Z.Y. Cui, *Corros. Sci.* 158, 108089 (2019).
41. BS EN ISO 17081-2014.
42. H.H. Johnson, N. Quick, and A.J. Kumnick, *Scr. Metall.* 13, 67 (1979).
43. A.M. Brass, F. Guillon, and S. Vivet, *Metall. Mater. Trans. A* 35A, 1449 (2004).

44. S.Z. Wang, Z.J. Gao, G.L. Wu, and X.P. Mao, *Int. J. Min. Met. Mater.* 29, 645 (2022).
45. Y. Han, J. Shi, L. Xu, W.Q. Cao, and H. Dong, *Mater. Des.* 34, 427 (2012).
46. C.D. Beachem, *Metall. Trans. A* 3, 441 (1972).

Publisher's Note Springer Nature remains neutral with regard to jurisdictional claims in published maps and institutional affiliations.

Springer Nature or its licensor (e.g. a society or other partner) holds exclusive rights to this article under a publishing agreement with the author(s) or other rightsholder(s); author self-archiving of the accepted manuscript version of this article is solely governed by the terms of such publishing agreement and applicable law.